molecules

MDPI

Article

CeO_2-Supported TiO_2−Pt Nanorod Composites as Efficient Catalysts for CO Oxidation

Haiyang Wang [1,†], Ruijuan Yao [1,†], Ruiyin Zhang [1], Hao Ma [1], Jianjing Gao [1], Miaomiao Liang [2], Yuzhen Zhao [1] and Zongcheng Miao [1,3,*]

[1] Xi'an Key Laboratory of Advanced Photo-Electronics Materials and Energy Conversion Device, School of Electronic Information, Xijing University, Xi'an 710123, China
[2] School of Materials Science and Engineering, Xi'an Polytechnic University, Xi'an 710048, China
[3] School of Artificial Intelligence, Optics and Electronics (iOPEN), Northwestern Polytechnical University, Xi'an 710072, China
* Correspondence: miaozongcheng@nwpu.edu.cn
† These authors contributed equally to this work.

Abstract: Supported Pt-based catalysts have been identified as highly selective catalysts for CO oxidation, but their potential for applications has been hampered by the high cost and scarcity of Pt metals as well as aggregation problems at relatively high temperatures. In this work, nanorod structured (TiO_2−Pt)/CeO_2 catalysts with the addition of 0.3 at% Pt and different atomic ratios of Ti were prepared through a combined dealloying and calcination method. XRD, XPS, SEM, TEM, and STEM measurements were used to confirm the phase composition, surface morphology, and structure of synthesized samples. After calcination treatment, Pt nanoparticles were semi-inlayed on the surface of the CeO_2 nanorod, and TiO_2 was highly dispersed into the catalyst system, resulting in the formation of (TiO_2−Pt)/CeO_2 with high specific surface area and large pore volume. The unique structure can provide more reaction path and active sites for catalytic CO oxidation, thus contributing to the generation of catalysts with high catalytic activity. The outstanding catalytic performance is ascribed to the stable structure and proper TiO_2 doping as well as the combined effect of Pt, TiO_2, and CeO_2. The research results are of importance for further development of high catalytic performance nanoporous catalytic materials.

Keywords: Al-Ce−Pt-TiO_2 alloy ribbon; dealloying; CO oxidation; (TiO_2−Pt)/CeO_2

Citation: Wang, H.; Yao, R.; Zhang, R.; Ma, H.; Gao, J.; Liang, M.; Zhao, Y.; Miao, Z. CeO_2-Supported TiO_2−Pt Nanorod Composites as Efficient Catalysts for CO Oxidation. *Molecules* **2023**, *28*, 1867. https://doi.org/10.3390/molecules28041867

Academic Editors: Waseem Raza, Xingke Cai and Arshad Hussain

Received: 18 January 2023
Revised: 4 February 2023
Accepted: 9 February 2023
Published: 16 February 2023

1. Introduction

Carbon monoxide is one of the most dangerous waste gases because of its harmful impact on the environment and high toxicity to animal and human lives. As catalytic CO oxidation is an efficient method to eliminate CO pollution under low temperature conditions, it has attracted widespread research interest in recent years [1,2]. Among them, the supported Pt-based catalysts have been widely investigated since Langmuir's first discovery [3–5]. Pt-based catalysts are critical to industrial CO oxidation because of their superior catalytic activity and stable catalytic properties [6–8]. The catalytic mechanism of Pt catalysts has been widely investigated and the results show that the reaction generally follows Langmuir–Hinshelwood (L-H) models [9–11]. However, the relative high cost and scarcity of noble metals, as well as their aggregation tendency as temperature rises, have retarded their further development [12,13]. Both theoretical and experimental studies have demonstrated that combining transition metal oxides [14,15] or rare earth metal ions [16,17] with noble metals is an effective method to reduce cost while maintaining stable catalytic property, which has been widely used in fuel cell and energy conversion/storage equipment. TiO_2, as a typical metal oxide, exhibits high oxygen storage capacity and redox properties as well as active catalytic performance by enhancing the migration rate of surface-active oxygen atoms and plays an important role in the catalysis field [18–20]. For example, Liou's

team [21] prepared Cu-doped TiO_2 microsphere for catalytic CO oxidation. They think that the highly dispersed doping metals can increase the exposure of copper and TiO_2 matrix, thus leading to the improvement of catalytic performance. However, the bulk metal oxides always show poor charge transfer ability and conductivity, which hinders their full play. Combining TiO_2 with Pt is an effective strategy to avoid the aggregation of Pt and enhance the overall property of materials. Liu's group [22] fabricated the Pt-Au/TiO_2-CeO_2 catalyst and found that the introduction of TiO_2 into a system can improve CO oxidation by enhancing the charge transfer from Pt to Au sites. Nava's team [23] investigated the loading amount of TiO_2 on catalytic performance of Au/TiO_2/SBA-15 systems and concluded that the catalyst reached the highest catalytic activity when 10 wt% TiO_2 was added. Therefore, TiO_2 is a good promoter in improving the catalytic performance of catalysts.

In practice, the metallic catalysts or metal–metal oxide composites are always supported on some nanostructured substrates to form heterogeneous catalysts [24]. This unique structure can allow good dispersion of noble metals and make full play use of the catalysts. It is well established that the noble catalysts supported on reducible metal oxides are more active than non-reducible oxides such as Al_2O_3 or SiO_2 [25,26]. In comparison, as a unique rare metal oxide, CeO_2 has been applied as a superior reducible supporting oxide due to its rich reservation and fast storage/release oxygen ability [27]. More importantly, the reversible Ce^{3+}/Ce^{4+} redox reaction and easy generation of oxygen vacancies in CeO_2 can contribute to the improvement in CO oxidation rate [28,29]. Previous studies also imply that the morphology and facets of CeO_2-based nanocomposites can greatly influence the formation and migration of surface oxygen vacancies, and nanosized structured CeO_2 materials, including nanospheres, nanorods, and nanocubes [30,31], have been synthesized. Among these structures, nanorod-shaped CeO_2 has received a substantial amount of attention because of its potentially large surface area and abundance of oxygen vacancy defects. Li et al. [32] prepared Au cluster-CeO_2 catalysts and concluded that the Au25 nanoclusters on CeO_2 nanorods and nano polyhedra display higher activity than CeO_2 nanocubes due to the difference in concentration of (O) species on ceria surface. Kwangjin An's group [33] fabricated Pt/CeO_2 with different morphologies and found that the Pt/CeO_2 with cube morphology shows the best activity compared with other structured samples. It is therefore predicated that the catalytic activity of CeO_2-based catalysts can be controlled by tuning their physicochemical properties. However, the conventional fabrication methods always require relatively high cost and complicated or time-consuming preparation processes, which limit their large-scale application.

The structure and activity of a catalyst is greatly related to the synthesis method. Compared with the traditional preparation method, dealloying is a simple and pollution-free method to fabricate three-dimensional nanoporous materials on a large-scale production basis [34]. The structure and pore size of samples can also be controlled by adjusting the dealloying temperature or composition of precursor alloys [35]. Metal oxides such as NiO [36] and CuO [37] or noble metals such as Ag [38], Au [39], and Pt [6] have been reported to be successfully supported on CeO_2 and have displayed satisfying catalytic activity. Whereas the Pt/TiO_2 composites supported onto CeO_2 to improve catalytic activity has been rarely reported.

Herein, the nanorod structured (TiO_2−Pt)/CeO_2 catalysts with the addition of Pt and varied amount of TiO_2 were fabricated through a combined dealloying and calcination method. The highly dispersed Pt and TiO_2 nanoparticles are loaded onto CeO_2 and form a nanoscale interface, which can accelerate the movement rate of electrons at the interface. The good framework structure also makes CO access catalysts more efficiently and gives full play to the role of active phases. The ($0.5TiO_2$−Pt)/CeO_2 catalyst shows optimal catalytic property of 50% and 99% at reaction temperatures as low as 55 °C and 90 °C, respectively. This work provides a new idea for preparation of high catalytic performance transition metal/CeO_2-based catalysts for large-scale production.

2. Results and Discussion

2.1. Characterization of Catalysts

Figure 1a displays the XRD patterns of melt-spun and dealloyed $Al_{91.2}Ce_8Pt_{0.3}Ti_{0.5}$ ribbons. As observed, the melt-spun $Al_{91.2}Ce_8Pt_{0.3}Ti_{0.5}$ ribbons consisted of α-Al, Al_4Ce and $Al_{92}Ce_8$ phases; after the dealloying procedure, only a new phase of CeO_x was detected while α-Al, Al_4Ce, and $Al_{92}Ce_8$ phases disappeared, implying that most of the Al has been removed. The diffraction peaks representing Pt/Ti cannot be detected, which is ascribed to their low content and high dispersion into alloy ribbons. The XRD patterns of $Al_{91.4}Ce_8Pt_{0.3}Ti_{0.3}$, $Al_{91.2}Ce_8Pt_{0.3}Ti_{0.5}$, and $Al_{91}Ce_8Pt_{0.3}Ti_{0.7}$ melt-spun ribbons after dealloying and calcination treatments are displayed in Figure 1b. The diffraction at 28.5°, 32.9°, 47.4°, 56.2°, 69.2°, and 76.7° corresponded to the (111), (200), (220), (311), (400), and (331) planes of cubic CeO_2 (PDF#89-8436), respectively; the weak diffraction peak at 41° representing Pt was also discovered while no peaks related to Ti was found. However, the content of Al, Ce, Pt, and Ti in the $(0.5TiO_2$-Pd)/CeO_2 catalyst obtained from $Al_{91.2}Ce_8Pt_{0.3}Ti_{0.5}$ melt-spun ribbon is 3.81 at%, 90.14 at%, 1.66 at%, and 4.4 at%, respectively, as shown in the EDS spectrum in Figure S1, demonstrating that Pt and Ti have been added into Al-Ce precursor alloys successfully.

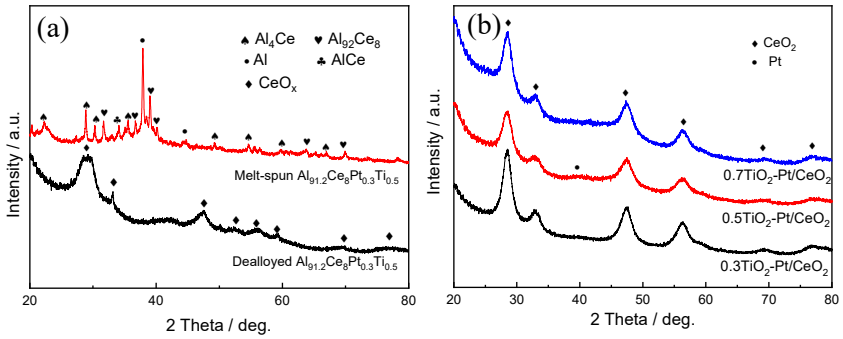

Figure 1. The XRD patterns of (**a**) melt-spun and dealloyed $Al_{91.2}Ce_8Pt_{0.3}Ti_{0.5}$ ribbons; (**b**) $(xTiO_2-Pt_{0.3})/CeO_2$ (X = 0.3, 0.5, 0.7) calcined at 300 °C.

To further confirm the chemical state of Pt, Ti, and Ce, XPS characterization of $(0.5TiO_2-Pt)/CeO_2$ is conducted with results shown in Figure 2. The Ce 3d spectrum displayed in Figure 2a reveals that the sample exhibits both Ce^{4+} and Ce^{3+} ions. The five peaks at 881.9 eV, 888.3 eV, 897.7 eV, 900.4 eV, and 907.3 eV are ascribed to Ce^{4+}, while the other two peaks at 885.1 eV and 903.7 eV corresponded to Ce^{3+}. The existence of Ce^{3+} implies the generation of oxygen vacancies; Ce^{3+} can adsorb active oxygen at the catalytic interface, thus contributing to the formation of interfacial active center. The concentration of Ce^{3+} can be reflected from the integrated areas of the Ce^{3+} peak to the total (Ce^{3+} + Ce^{4+}) peaks. As a result, the surface concentration of Ce^{3+} on the $(0.5TiO_2-Pt)/CeO_2$ catalyst is 21.58% according to the fitting calculation of the Ce 3d spectrum. For the Pt 4f spectrum in Figure 2b, the binding energies at 70.8 eV for Pt $4f_{7/2}$ and 73.9 eV for Pt $4f_{5/2}$ are assigned to metallic state platinum (Pt^0), while the peaks at 71.9 eV and 76.4 eV corresponded to Pt^{2+} [40,41]. Likewise, the content of Pt^0 accounts for 61.6% of the total (Pt^0 + Pt^{2+}). The Ti 2p spectrum in Figure 2c displays a Ti^{4+} binding energy, in which the two peaks at 463.6 eV and 457.8eV corresponded to Ti $2p_{1/2}$ and Ti $2p_{3/2}$, respectively [42]. Since Ti mainly existed in the form of Ti^{4+} in the product, it is deduced that TiO_2 existed in the composite material. The O 1s spectrum in Figure 2d can be fitted to three peaks. The binding energies centered around ~529.3 eV, ~531 eV, and ~532.2 eV corresponded to lattice oxygen species (O_{lat}), surface adsorbed oxygen (O_{sur}), and weakly bonded specific oxygen species such as adsorbed O_2, H_2O, and CO_2 (O_{bon}), respectively. The active surface oxygen can be evaluated by O_{sur}, and the ratio of active oxygen species for $(0.5TiO_2-Pt)/CeO_2$ is 20.8%.

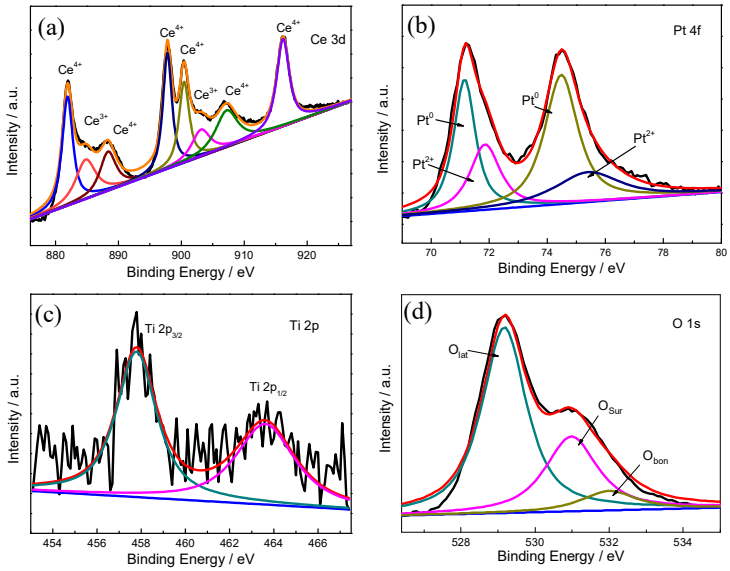

Figure 2. XPS spectra of (**a**) Ce 3d, (**b**) Pt 4f, (**c**) Ti 2p, and (**d**) O 1s of the $(0.5TiO_2-Pt)/CeO_2$ catalyst.

Figure 3 presents the surface and cross-sectional morphologies of $(TiO_2-Pt)/CeO_2$ with different TiO_2 content. As observed, all the three samples display a robust framework, which are composed of a nanoporous matrix with nanorods embedded in them. The nanorods pile up on each other to form rich pores among them. Notably, the slight increase in TiO_2 content from 0.3 at% to 0.5 at% does not influence the overall morphologies of samples and only fine-tunes the arrangement of pores, as shown in Figure 3a,d,g. Moreover, the cross-sectional SEM image of $(0.5TiO_2-Pt)/CeO_2$ in Figure S2 further reflects the presence of rich pores and independent arrangement of nanorods. The unique and robust nanorod-embedded matrix structure is beneficial to stabilize the overall structure of samples during the catalytic process; the existence of lots of pores distributed among matrix and nanorods can also provide more channels for reacted gas to enter and exit; therefore, the catalytic CO oxidation performance is expected to be improved.

TEM and HRTEM characterization are performed to further understand the microstructure of $(TiO_2-Pt)/CeO_2$ catalysts. As shown in the TEM images of $(0.3TiO_2-Pt)/CeO_2$, $(0.5TiO_2-Pt)/CeO_2$, and $(0.7TiO_2-Pt)/CeO_2$ presented in Figure 3b,e,h, respectively, the samples are composed of a large number of uniform nanorods with an average diameter of 10 nm, which are interconnected and stacked on each other; some dark nanoparticles with diameter of 3–5 nm on average are uniformly embedded on the surface of nanorods. These are consistent with SEM results. The corresponding HRTEM images of $(0.3TiO_2-Pt)/CeO_2$, $(0.5TiO_2-Pt)/CeO_2$, and $(0.7TiO_2-Pt)/CeO_2$ are displayed in Figure 3c,f,i, respectively. The lattice fringe with a space of 0.32 nm corresponded to the (111) plane of CeO_2, implying the cubic structured CeO_2 nanorod in the (111) crystal plane. The dark nanoparticles with lattice space of 0.229 nm are assigned to the (111) plane of Pt, which further indicates that Pt has been added into Al-Ce alloy successfully. However, no results related to Ti are found in TEM characterization. This may be because the calcination temperature in the $(TiO_2-Pt)/CeO_2$ system is relatively low (300 °C); CeO_2 can inhibit the crystallization of other oxides during the calcination process under such low temperatures [43]. Our previous work also found that CeO_2 can inhibit the crystallization of NiO; as temperature rises, the structure of NiO in the system is transformed from the amorphous state into the crystallization state [36]. Therefore, the reason why the lattice fringe related to TiO_2 is not detected in TEM characterization may be the amorphous state of TiO_2 in the system, which is in line with XRD results.

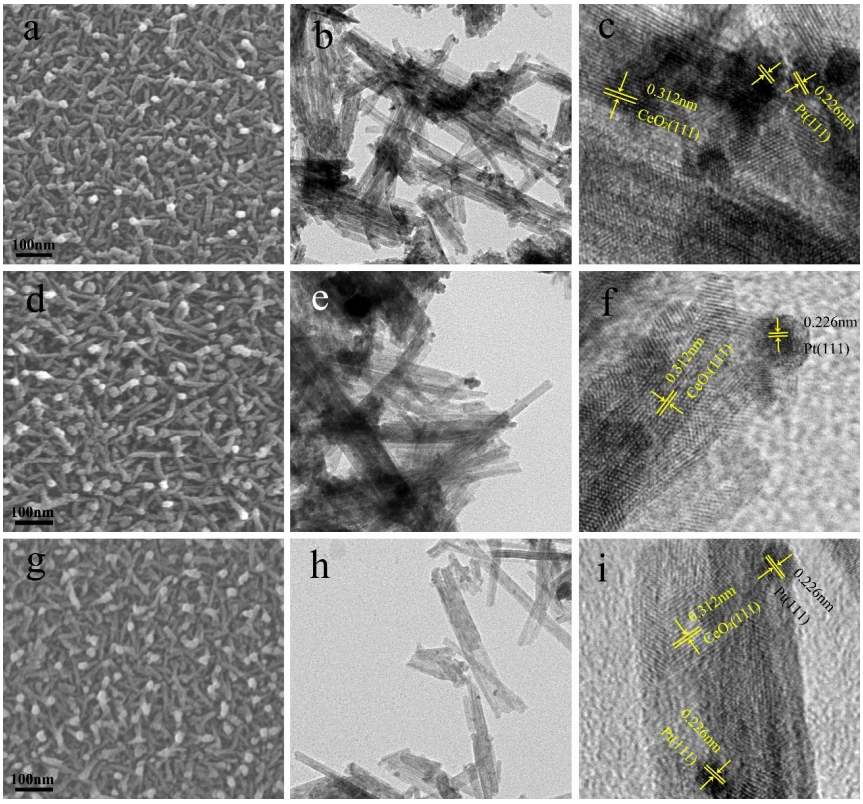

Figure 3. The SEM images of (**a**) $(0.3TiO_2-Pt)/CeO_2$, (**d**) $(0.5TiO_2-Pt)/CeO_2$, and (**g**) $(0.7TiO_2-Pt)/CeO_2$; the TEM and HRTEM images of (**b**,**c**) $(0.3TiO_2-Pt)/CeO_2$, (**e**,**f**) $(0.5TiO_2-Pt)/CeO_2$, and (**h**,**i**) $(0.7TiO_2-Pt)/CeO_2$.

The distribution of elements on the surface of the CeO_2 nanorod is further investigated via STEM mapping, with results presented in Figure 4. Figure 4a displays the SEM image of $(0.5TiO_2-Pt)/CeO_2$. For $(0.5TiO_2-Pt)/CeO_2$ obtained from $Al_{91.2}Ce_8Pt_{0.3}Ti_{0.5}$ through the dealloying and calcination processes, Pt is semi-embedded onto the surface of the CeO_2 nanorod, while Ti is uniformly distributed into the CeO_2 nanorod, as reflected in Figure 4b–d. Combined with XPS and STEM results, it can be concluded that Ti mainly exists as the TiO_2 phase in the composite system; thus, the obtained composite material is named as $(TiO_2-Pt)/CeO_2$.

The specific surface area, pore size distribution, and pore volume of $(TiO_2-Pt)/CeO_2$ composite materials with varied TiO_2 proportions are measured via the N_2 adsorption-desorption test, with results displayed in Figure 5. The isotherms of three catalysts belong to type IV and possess H3 hysteresis loops at relative pressure of 0.7–1.0 P/P_0 according to the IUPAC classification (Figure 5a), indicating the mesoporous structure of $(TiO_2-Pt)/CeO_2$ [44]. The BET surface area of $(0.3TiO_2-Pt)/CeO_2$, $(0.5TiO_2-Pt)/CeO_2$, and $(0.7TiO_2-Pt)/CeO_2$ is 101.88, 108.88, and 110.11 $m^2\ g^{-1}$, respectively, while their corresponding pore size is centered at 14.36, 12.71, and 13.58 nm, and pore volume is 0.36, 0.37, and 0.35 $cm^3\ g^{-1}$, respectively, as displayed in the BHJ pore size distribution curves in Figure 5b. Obviously, the three catalysts possess similar results in specific surface area and pore size distribution, which illustrates that the variation in the amount of Pt and TiO_2 does not influence the physical structure of materials significantly, nor their mesoporous properties. In contrast, $(0.5TiO_2-Pt)/CeO_2$ has higher specific surface area, larger pore volume, and smaller porosity, which is beneficial for gas penetration during the catalytic process by providing more reaction paths and active sites for catalytic CO oxidation, and thus improving its catalytic performance.

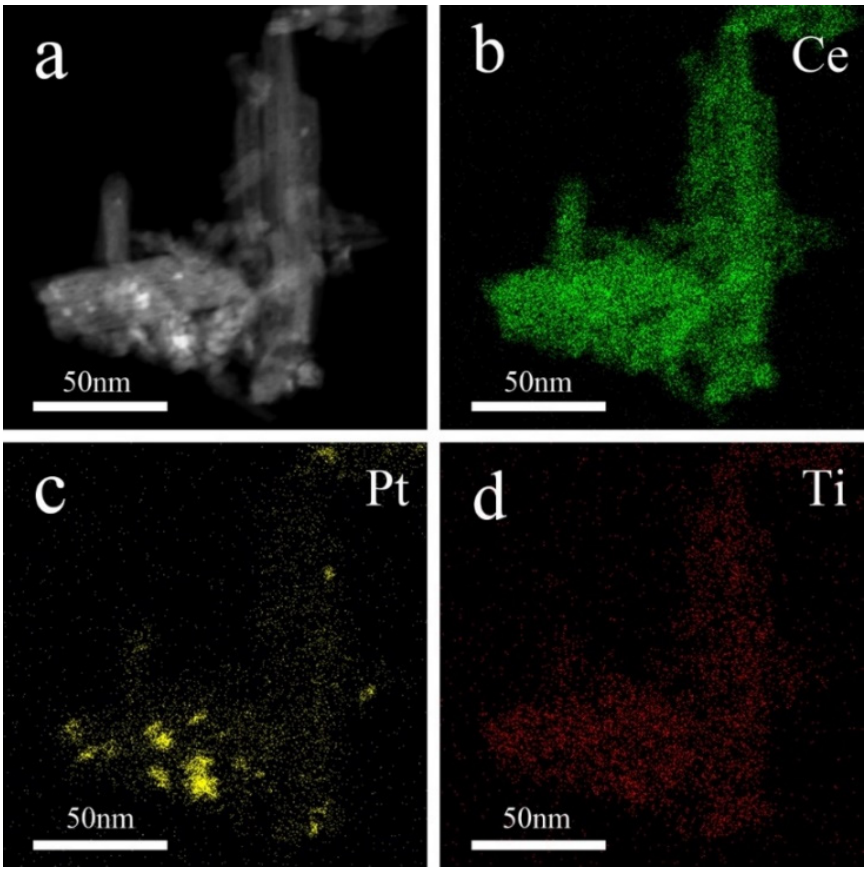

Figure 4. The STEM image of (**a**) $(0.5TiO_2-Pt)/CeO_2$ and element mapping of (**b**) Ce, (**c**) Pt, and (**d**) Ti.

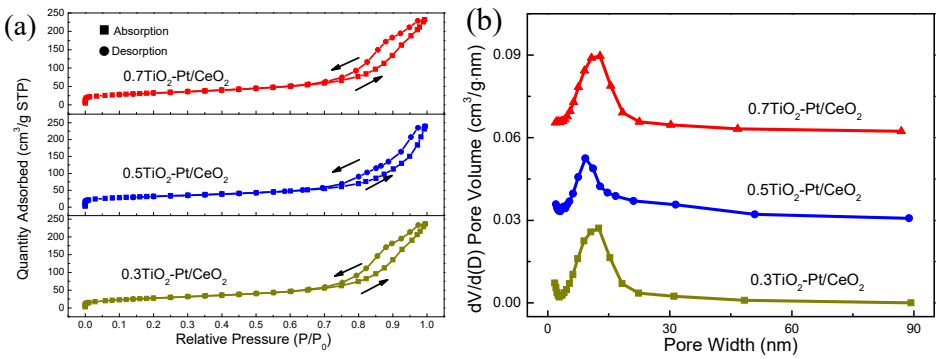

Figure 5. (**a**) Nitrogen adsorption–desorption isotherms and (**b**) the BHJ pore size distribution of $(TiO_2-Pt)/CeO_2$.

Raman spectroscopy measurement is conducted to understand the structural phase changes of $(TiO_2-Pt)/CeO_2$ catalysts. In Figure 6, the weak peaks of Raman shift around 306 and 534 cm^{-1} indicate the existence of anatase TiO_2; the appearance of new and broad peaks around 269 cm^{-1} is attributed to co-doping of Pt [45,46]. Moreover, compared with Raman peaks of pure CeO_2 in Figure S3, the diffraction peak is shifted from 459 cm^{-1} to 439 cm^{-1}, which is ascribed to the formation of more grain boundaries after the addition of TiO_2 and Pt nanoparticles. It is expected that the Pt and TiO_2 nanoparticles that are highly dispersed on CeO_2 nanorods can cause a large number of defects including oxygen vacancies, grain boundaries, and dislocations, which are helpful for improvement in catalytic activity of catalysts.

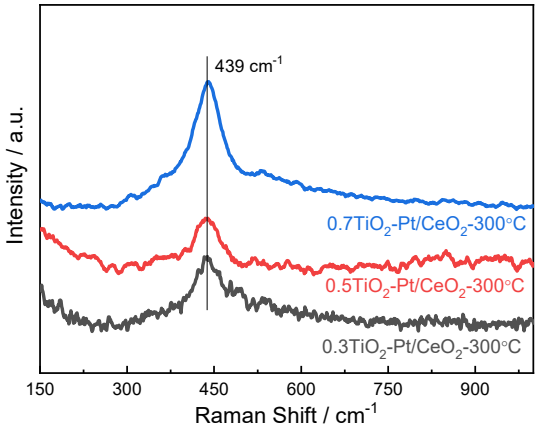

Figure 6. Raman spectra of $(TiO_2-Pt)/CeO_2$ catalysts.

2.2. Catalytic Performance

Figure 7 presents the catalytic CO oxidation performance of $(TiO_2-Pt)/CeO_2$ catalysts. For $Pt_{0.3}/CeO_2$ without the addition of TiO_2, the temperature for 50% CO conversion (T_{50}) and 99% CO conversion (T_{99}) is 91°C and 113 °C, respectively, which is much higher than that of the CeO_2 matrix (T_{50} = 235 °C, T_{99} = 320 °C), as observed in Figure S4. The catalytic activity is greatly improved after the addition of TiO_2. The T_{50} and T_{99} of $(0.3TiO_2-Pt)/CeO_2$ is 65 °C and 110 °C, respectively, when 0.3 at% Ti is added into alloy system. As Ti content increases to 0.5 at%, the catalytic activity reaches the optimum with a T_{50} and T_{99} decrease to 55 °C and 90 °C, respectively; on further increasing Ti content to 0.7 at%, catalytic performance decreases with T_{50} and T_{99} of 65 °C and 100 °C, respectively, as displayed in Figure 7a. The influence of calcination temperature on catalytic property of the $(0.5TiO_2-Pt)/CeO_2$ catalyst is shown in Figure 7b, in which the T_{99} of $(0.5TiO_2-Pt)/CeO_2$ without calcination treatment, calcined at 200 °C, 300 °C, 400 °C, and 500 °C is 120 °C, 110 °C, 90 °C, 100 °C, and 120 °C, respectively. The catalytic performance of $(0.5TiO_2-Pt)/CeO_2$ was stable after three repeated tests (Figure S5), implying good reusability of $(0.5TiO_2-Pt)/CeO_2$. The catalytic activity of $(0.5TiO_2-Pt)/CeO_2$ also surpasses the state-of-the-art TiO_2/CeO_2-based catalysts reported in the literature, as shown in Table 1 [24,47–50], indicating its superior catalytic property. It is clearly observed that the catalytic activity is improved as calcination temperature increases from room temperature to 300 °C, which is reduced as calcination temperature further increases. The $(0.5TiO_2-Pt)/CeO_2$ exhibits optimum catalytic performance after calcination at 300 °C. Furthermore, the addition of Ti into the Pt-CeO_2 catalytic system can partly make up for the deficiency of the single precious metal Pt and realize the purpose of the experiment.

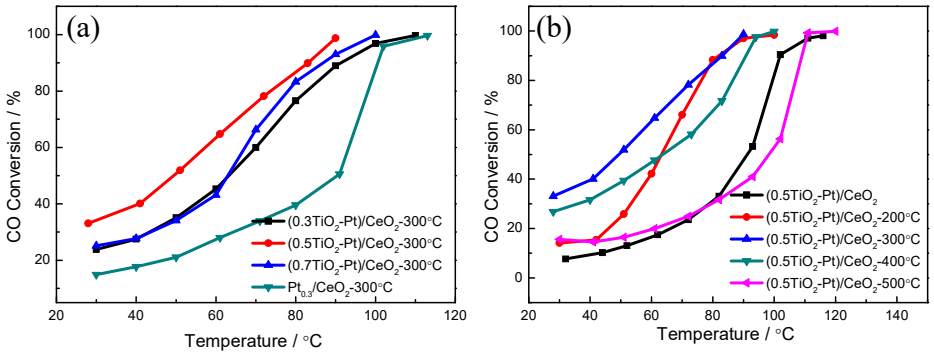

Figure 7. (**a**) The catalytic performance of $Pt_{0.3}/CeO_2$, $(0.3TiO_2-Pt)/CeO_2$, $(0.5TiO_2-Pt)/CeO_2$, $(0.7TiO_2-Pt)/CeO_2$ catalysts; (**b**) the $(0.5TiO_2-Pt)/CeO_2$ catalyst obtained at different calcination temperatures.

Table 1. Comparison on catalytic performance of $(0.5TiO_2-Pt)/CeO_2$ with previous reports.

Sample	PreparationMethod	Test Condition	T_{50} (°C)	T_{99} (°C)	Reference
Pd/Pr-CeO_2-5%	Hydrothermal synthesis	1% CO, 99% dry air	/	160	[24]
Pt/CeO_2	Electrostatic Adsorption	1% CO, 20% O_2, He balance	140	/	[47]
Ir/CeO_2	wet chemical reduction	1% CO	/	110	[48]
Au/TiO_2-S	Deposition-precipation method	2.0% CO, 8% O_2, He balance	/	20	[49]
Co_3O_4@CeO_2	Hydrothermal method	1% CO, 99% air	/	160	[50]
$(0.5TiO_2-Pt)/CeO_2$	Dealloying and calcination	1% CO, 10% O_2, 89% N_2	55	90	This work

The catalytic performance of $(0.5TiO_2-Pt)/CeO_2$ as a function of flow rate at 70 °C is detected, with corresponding catalytic activities shown in Figure 8a. As the total gas flow rate increases from 40 to 120 mL min^{-1}, the CO conversion decreases from 97% to 58%. It can be also clearly detected that the reaction rate is positively related to flow rate. Figure 8b further explores the influence of O_2 concentration in feed gas on catalytic performance of $(0.5TiO_2-Pt)/CeO_2$. The test temperature is kept at 90 °C with a flow rate of 100 mL min^{-1}. The CO conversion rate can reach 99% as 10% O_2 is initially infused into the system thanks to the sufficient O_2 environment; CO conversion rate is reduced first and then kept stable at 10% when O_2 supply is suddenly decreased to zero, which may be ascribed to the existence of surface lattice oxygen that can migrate to active sites and combine with adsorbed CO to form oxygen vacancies. However, CO conversion rate increases in poor oxygen conditions (0.3–5% O_2) and then recovers to initial 99% value and stays unchanged when O_2 is resupplied into feed gas, implying the superior catalytic CO oxidation property of $(0.5TiO_2-Pt)/CeO_2$.

The long-term stability of the $(0.5TiO_2-Pt)/CeO_2$ catalyst is also evaluated to investigate its practical application potential, as shown in Figure 9a. The $(0.5TiO_2-Pt)/CeO_2$ catalyst exhibits above 95% CO conversion under mixed atmosphere (1% CO, 10% O_2, 89% N_2) and is stable without deterioration after successive reaction of 55 h, indicating outstanding catalytic activity of the nanorod-shaped $(0.5TiO_2-Pt)/CeO_2$ catalyst. The outstanding catalytic performance of the $(TiO_2-Pt)/CeO_2$ catalyst can be attributed to the unique structure and phase composition. The existence of Ce^{3+} on catalytic interface can adsorb active oxygen, which is conducive to the formation of the interfacial active center; highly dispersed TiO_2 can accelerate the migration rate of active oxygen species on the surface of CeO_2 so that the oxygen atoms can react with activated CO to form CO_2 [36], as reflected in the mechanism diagram in Figure 9b. The introduction of Pt nanoparticles and highly dispersed TiO_2 can form a large number of nanoscale interfaces, which greatly promotes the movement of electrons at the interface. The electrons can not only activate the CO gas adsorbed by noble metals quickly but also accelerate the dissociation of generated CO_2 on the catalyst surface, thus ultimately making the reaction rate increase. In addition, the robust framework structure provides a place for catalysts to contact harmful gases effectively; it also stimulates the effect of noble metals that are loaded on the CeO_2 structure and inhibits the agglomeration or growth of loaded nanoparticles during heating or catalytic processes, guaranteeing the high catalytic stability of the catalysts.

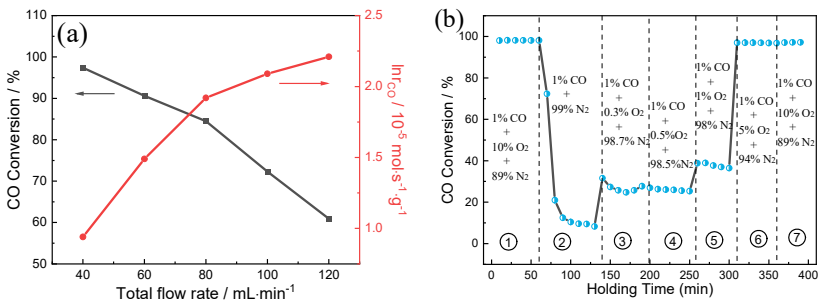

Figure 8. (**a**) Catalytic activity of $(0.5TiO_2-Pt)/CeO_2$ under different space velocities at 70 °C. The measurement was performed using 100 mg of the catalyst with a mixed gas of 1% CO, 10% O_2, and rest N_2 at a flow rate ranging from 40 to 120 mL min^{-1}. (**b**) Catalytic performance under varied oxygen concentrations.

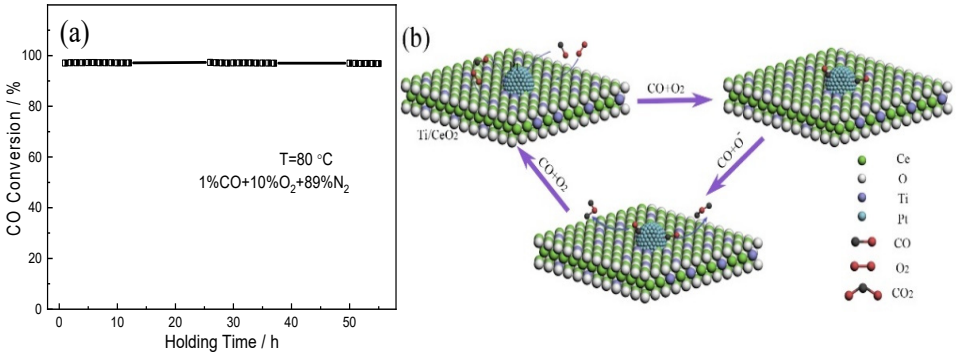

Figure 9. (**a**) The long-term stability of the $(0.5TiO_2-Pt)/CeO_2$ catalyst; (**b**) a possible mechanism for reaction of CO on the $(TiO_2-Pt)/CeO_2$ catalyst.

3. Materials and Methods

3.1. Material Preparation

The $Al_{92}Ce_8$, $Al_{91.7}Ce_8Pt_{0.3}$, $Al_{91.4}Ce_8Pt_{0.3}Ti_{0.3}$, $Al_{91.2}Ce_8Pt_{0.3}Ti_{0.5}$, and $Al_{91}Ce_8Pt_{0.3}Ti_{0.7}$ alloys were achieved from pure Al, Ce, Pt, and Pd through the arc-melting method under high-purity Ar atmosphere. After being remelted and solidified, the Al-Ce−Pt-Ti alloy ribbons with 4–6 mm width and 40–70 μm thickness were prepared. The quenched alloy ribbons were dealloyed in 20 wt% NaOH aqueous solution at room temperature for 2 h until no obvious bubbles were generated and most of Al were removed. After this, the samples were then further corroded at 80 °C for 10 h. Finally, after cleaning and drying, the dealloyed samples were calcined at 200–500 °C for 2 h under pure O_2 environment.

3.2. Characterization

X-ray diffraction patterns were collected on Bruker D8 Advance to analysis phase composition. Field emission scanning electron microscopy (FESEM, JEOL, JSM-7000F) and high-resolution transmission electron microscopy (HRTEM, JEOL, JEM-2100) were employed to characterize surface morphologies and microstructures. A scanning transmission electron microscope (STEM, FEI-200) equipped with an Oxford Instruments EDS spectrometer was utilized to conduct EDS analysis and mapping. X-ray photoelectron spectroscopy (XPS) was performed on ESCALAB Xi+ to confirm element composition and valence state. Nitrogen sorption was tested on Micromeritics ASAP 2020 at 77 K, and the Barrett–Joyner–Halenda algorithm was adopted to evaluate pore size and pore volume. Raman spectra were collected on an HR 800 fully automatic laser Raman spectrometer.

3.3. Catalytic Evaluations

The catalytic activity was detected in a tubular reactor at atmospheric pressure. A 100 mg sample was added to the reactor and fixed with quartz wool. The mixed reaction gas consisting of 1% CO, 10% O_2, and 89% N_2 (volume fraction) was entered into the test system at a flow rate of 100 mL min^{-1} (space velocity 60,000 h^{-1}). The inflowed and outflowed gases were collected using an Anglit 7890B gas chromatograph equipped with a hydrogen flame detector (FID). The CO conversion was determined by:

$$\text{CO conversion} = \frac{C_{in} - C_{out}}{C_{in}} \times 100\% \quad (1)$$

where C_{in} and C_{out} stand for the concentration of the CO inlet and outlet of the reactor, respectively.

4. Conclusions

In conclusion, the nanorod structured $(TiO_2-Pt)/CeO_2$ catalysts are fabricated via the combined dealloying and calcination method. SEM, TEM, and STEM measurements imply that the Pt nanoparticles were semi-inlayed on the surface of the CeO_2 nanorod, while TiO_2 were highly dispersed into the catalyst system. By rationally adjusting the proportion of

TiO_2 in the system, the obtained $(0.5TiO_2-Pt)/CeO_2$ displays unique nanorod structure and large pore volume, which contributes to exceptional catalytic activity with T_{50} and T_{99} temperature as low as 55 °C and 90 °C, respectively. It is considered that the stable structure, proper TiO_2 doping, and jointed effect of Pt and TiO_2 as well as rich nanopores contribute to the enhanced catalytic performance of $(TiO_2-Pt)/CeO_2$ catalysts. This work provides a new idea and facile strategy for the fabrication of noble metal/metal oxide composites with high catalytic performance.

Supplementary Materials: The following supporting information can be downloaded at https://www.mdpi.com/article/10.3390/molecules28041867/s1, Figure S1: The EDS spectrum of Al91.2Ce8Pt 0.3Ti0.5 melt-spun ribbons after dealloying and calcination treatment. Figure S2: The cross-sectional SEM image of $(0.5TiO_2-Pt)/CeO_2$. Figure S3: The Raman spectrum of pure CeO_2. Figure S4: The catalytic performance of CeO_2 matrix. Figure S5: The reusability test of $(0.5TiO_2-Pt)/CeO_2$.

Author Contributions: H.W. conceived the idea and directed the experiments. R.Y. fabricated all of the samples. R.Z., H.M. and J.G. conducted the characterizations. M.L. and Y.Z. analyzed the data. H.W. drafted the manuscript, and Z.M. revised it. All authors have read and agreed to the published version of the manuscript.

Funding: This work was supported by the National Natural Science Foundation of China (Grant No. 52173263), the Regional Innovation Capability Guidance Program of Shaanxi (No. 2022QFY03-02), the Natural Science Foundation of Anhui Province, China (No. 2108085J11), Natural Science Basic Research Plan in Shaanxi Province of China (Program No. 2022JQ-139), the Scientific Research Program Funded by Shaanxi Provincial Education Department (22JK0590, 22JP100), the Fundamental Research Funds for the Central Universities, Northwestern Polytechnical University (No. D5000210825), the Scientific research fund for high-level talents of Xijing University (No. XJ21B17), and the Youth Innovation Team of Shaanxi Universities.

Institutional Review Board Statement: Not applicable.

Informed Consent Statement: Not applicable.

Data Availability Statement: The raw data are available from the corresponding author upon reasonable request.

Acknowledgments: All authors are grateful for the financial support of this work provided by the Natural Science Foundation. The authors also thank his outstanding contributions in language polishing.

Conflicts of Interest: The authors declare no conflict of interest.

Sample Availability: Samples of the compounds are not available from the authors.

References

1. Wang, L.N.; Li, X.N.; He, S.G. Recent research progress in the study of catalytic CO oxidation by gas phase atomic clusters. *Sci. China Mater.* **2019**, *63*, 892–902. [CrossRef]
2. Soliman, N.K. Factors affecting CO oxidation reaction over nanosized materials: A review. *J. Mater. Res. Technol.* **2019**, *8*, 2395–2407. [CrossRef]
3. Langmuir, I. The mechanism of the catalytic action of platinum in the reactions $2CO + O_2 = 2CO_2$ and $2H_2 + O_2 = 2H_2O$. *Trans. Faraday Soc.* **1922**, *17*, 621–654. [CrossRef]
4. Shakeel, A.; Rizwan, K.; Farooq, U.; Iqbal, S.; Altaf, A.A. Advanced polymeric/inorganic nanohybrids: An integrated platform for gas sensing applications. *Chemosphere* **2022**, *294*, 133772. [CrossRef] [PubMed]
5. Qasim, M.; Bashir, M.S.; Iqbal, S.; Mahmood, Q. Recent advancements in α-diimine-nickel and -palladium catalysts for ethylene polymerization. *Eur. Polym. J.* **2021**, *160*, 110783. [CrossRef]
6. Camposeco, R.; Torres, A.E.; Zanella, R. Influence of the Preparation Method of Au, Pd, Pt, and Rh/TiO_2 Nanostructures and Their Catalytic Activity on the CO Oxidation at Low Temperature. *Top. Catal.* **2022**, *65*, 798–816. [CrossRef]
7. Lin, J.; Wang, X.; Zhang, T. Recent progress in CO oxidation over Pt-group-metal catalysts at low temperatures. *Chin. J. Catal.* **2016**, *37*, 1805–1813. [CrossRef]
8. Feng, C.; Liu, X.; Zhu, T.; Tian, M. Catalytic oxidation of CO on noble metal-based catalysts. *Environ. Sci. Pollut. Res. Int.* **2021**, *28*, 24847–24871. [CrossRef]
9. Therrien, A.J.; Hensley, A.J.R.; Marcinkowski, M.D.; Zhang, R.; Lucci, F.R.; Coughlin, B.; Schilling, A.C.; McEwen, J.S.; Sykes, E.C.H. An atomic-scale view of single-site Pt catalysis for low-temperature CO oxidation. *Nat. Catal.* **2018**, *1*, 192–198. [CrossRef]

10. Wang, Y.; Ma, J.; Wang, X.; Zhang, Z.; Zhao, J.; Yan, J.; Du, Y.; Zhang, H.; Ma, D. Complete CO Oxidation by O_2 and H_2O over Pt-$CeO_{2-\delta}$/MgO Following Langmuir-Hinshelwood and Mars-van Krevelen Mechanisms, Respectively. *ACS Catal.* **2021**, *11*, 11820–11830. [CrossRef]
11. Chen, Y.; Feng, Y.; Li, L.; Liu, J.; Pan, X.; Liu, W.; Wei, F.; Cui, Y.; Qiao, B.; Sun, X.; et al. Identification of Active Sites on High-Performance Pt/$A_{l2}O_3$ Catalyst for Cryogenic CO Oxidation. *ACS Catal.* **2020**, *10*, 8815–8824. [CrossRef]
12. Song, J.; Yang, Y.; Liu, S.; Li, L.; Yu, N.; Fan, Y.; Chen, Z.; Kuai, L.; Geng, B. Dispersion and support dictated properties and activities of Pt/metal oxide catalysts in heterogeneous CO oxidation. *Nano Res.* **2021**, *14*, 4841–4847. [CrossRef]
13. Song, H.C.; Han, G.; Reddy, K.P.; Choi, M.; Ryoo, R.; Park, J.Y. Synergistic interactions between water and the metal/oxide interface in CO oxidation on Pt/CeO_2 model catalysts. *Catal. Today*, 2022, *in press*. [CrossRef]
14. Dey, S.; Dhal, G.C.; Mohan, D.; Prasad, R. Advances in transition metal oxide catalysts for carbon monoxide oxidation: A review. *Adv. Compos. Hybrid Mater.* **2019**, *2*, 626–656. [CrossRef]
15. Bai, Y.; Huang, H.; Wang, C.; Long, R.; Xiong, Y. Engineering the surface charge states of nanostructures for enhanced catalytic performance. *Mater. Chem. Front.* **2017**, *1*, 1951–1964. [CrossRef]
16. Siakavelas, G.I.; Charisiou, N.D.; AlKhoori, A.; AlKhoori, S.; Sebastian, V.; Hinder, S.J.; Baker, M.A.; Yentekakis, I.V.; Polychronopoulou, K.; Goula, M.A. Highly selective and stable Ni/La-M (M=Sm, Pr, and Mg)-CeO_2 catalysts for CO_2 methanation. *J. CO2 Util.* **2021**, *51*, 101618. [CrossRef]
17. Zhang, Y.; Xu, J.; Xu, X.; Xi, R.; Liu, Y.; Fang, X.; Wang, X. Tailoring $La_2Ce_2O_7$ catalysts for low temperature oxidative coupling of methane by optimizing the preparation methods. *Catal. Today* **2020**, *355*, 518–528. [CrossRef]
18. Shutilov, A.A.; Zenkovets, G.A.; Kryukova, G.N.; Gavrilov, V.Y.; Paukshtis, E.A.; Boronin, A.I.; Koshcheev, S.V.; Tsybulya, S.V. Effect of the microstructure of Pt/CeO_2-TiO_2 catalysts on their catalytic properties in CO oxidation. *Kinet. Catal.* **2011**, *49*, 271–278. [CrossRef]
19. Cai, J.; Yu, Z.; Fan, X.; Li, J. Effect of TiO_2 Calcination Pretreatment on the Performance of Pt/TiO_2 Catalyst for CO Oxidation. *Molecules* **2022**, *27*, 3875. [CrossRef]
20. Yu, X.; Wang, Y.; Kim, A.; Kim, Y.K. Observation of temperature-dependent kinetics for catalytic CO oxidation over TiO_2-supported Pt catalysts. *Chem. Phys. Lett.* **2017**, *685*, 282–287. [CrossRef]
21. Yang, W.T.; Lin, C.J.; Montini, T.; Fornasiero, P.; Ya, S.; Liou, S.Y.H. High-performance and long-term stability of mesoporous Cu-doped TiO(2) microsphere for catalytic CO oxidation. *J. Hazard Mater.* **2021**, *403*, 123630. [CrossRef] [PubMed]
22. Hong, X.; Sun, Y.; Zhu, T.; Liu, Z. Pt-Au/MOx-CeO(2) (M = Mn, Fe, Ti) Catalysts for the Co-Oxidation of CO and H(2) at Room Temperature. *Molecules* **2017**, *22*, 351. [CrossRef] [PubMed]
23. Peza-Ledesma, C.L.; Escamilla-Perea, L.; Nava, R.; Pawelec, B.; Fierro, J.L.G. Supported gold catalysts in SBA-15 modified with TiO_2 for oxidation of carbon monoxide. *Appl. Catal. A Gen.* **2010**, *375*, 37–48. [CrossRef]
24. Deng, Y.; Tian, P.; Liu, S.; He, H.; Wang, Y.; Ouyang, L.; Yuan, S. Enhanced catalytic performance of atomically dispersed Pd on Pr-doped CeO_2 nanorod in CO oxidation. *J Hazard Mater* **2022**, *426*, 127793. [CrossRef] [PubMed]
25. Chen, K.; Wan, J.; Lin, J.; Zhou, R. Comparative study of three-way catalytic performance over Pd/CeO_2-ZrO_2-Al_2O_3 and Pd/La-Al_2O_3 catalysts: New insights into microstructure and thermal stability. *Mol. Catal.* **2022**, *526*, 112361. [CrossRef]
26. Wang, C.; Ren, D.; Du, J.; Qin, Q.; Zhang, A.; Chen, L.; Cui, H.; Chen, J.; Zhao, Y. In Situ Investigations on the Facile Synthesis and Catalytic Performance of CeO_2-Pt/Al_2O_3 Catalyst. *Catalysts* **2020**, *10*, 143. [CrossRef]
27. Konsolakis, M.; Lykaki, M. Facet-Dependent Reactivity of Ceria Nanoparticles Exemplified by CeO_2-Based Transition Metal Catalysts: A Critical Review. *Catalysts* **2021**, *11*, 452. [CrossRef]
28. Cam, T.S.; Omarov, S.O.; Chebanenko, M.I.; Izotova, S.G.; Popkov, V.I. Recent progress in the synthesis of CeO_2-based nanocatalysts towards efficient oxidation of CO. *J. Sci. Adv. Mater. Devices* **2022**, *7*, 100399. [CrossRef]
29. Trovarelli, A. Catalytic Properties of Ceria and CeO_2-Containing Materials. *Catal. Rev.* **1996**, *4*, 439–520. [CrossRef]
30. Zhou, K.; Wang, X.; Sun, X.; Peng, Q.; Li, Y. Enhanced catalytic activity of ceria nanorods from well-defined reactive crystal planes. *J. Catal.* **2005**, *229*, 206–212. [CrossRef]
31. Pan, C.; Zhang, D.; Shi, L.; Fang, J. Template-Free Synthesis, Controlled Conversion, and CO Oxidation Properties of CeO_2 Nanorods, Nanotubes, Nanowires, and Nanocubes. *Eur. J. Inorg. Chem.* **2008**, *15*, 2429–2436.
32. Li, Z.; Zhang, X.; Shi, Q.; Gong, X.; Xu, H.; Li, G. Morphology effect of ceria supports on gold nanocluster catalyzed CO oxidation. *Nanoscale Adv* **2021**, *3*, 7002–7006. [CrossRef] [PubMed]
33. Yoon, S.; Ha, H.; Kim, J.; Nam, E.; Yoo, M.; Jeong, B.; Kim, H.Y.; An, K. Influence of the Pt size and CeO_2 morphology at the Pt-CeO_2 interface in CO oxidation. *J. Mater. Chem. A* **2021**, *9*, 26381–26390. [CrossRef]
34. McCue, I.; Benn, E.; Gaskey, B.; Erlebacher, J. Dealloying and Dealloyed Materials. *Annu. Rev. Mater. Res.* **2016**, *46*, 263–286. [CrossRef]
35. Erlebacher, J. An Atomistic Description of Dealloying. *J. Electrochem. Soc.* **2004**, *151*, C614. [CrossRef]
36. Zhang, X.; Li, K.; Shi, W.; Wei, C.; Song, X.; Yang, S.; Sun, Z. Baize-like CeO_2 and NiO/CeO_2 nanorod catalysts prepared by dealloying for CO oxidation. *Nanotechnology* **2017**, *28*, 045602. [CrossRef]
37. Chen, K.; Zhao, X.; Zhang, X.J.; Zhang, W.S.; Wu, Z.F.; Wang, H.Y.; Han, D.X.; Niu, L. Enhanced photocatalytic CO_2 reduction by constructing an In_2O_3-CuO heterojunction with CuO as a cocatalyst. *Catal. Sci. Technol.* **2021**, *11*, 2713–2717. [CrossRef]
38. Li, G.; Zhang, X.; Feng, W.; Fang, X.; Liu, J. Nanoporous CeO2-Ag catalysts prepared by etching the CeO_2/CuO/Ag_2O mixed oxides for CO oxidation. *Corros. Sci.* **2018**, *134*, 140–148. [CrossRef]

39. Li, X.; Feng, J.; Perdjon, M.; Oh, R.; Zhao, W.; Huang, X.; Liu, S. Investigations of supported Au-Pd nanoparticles on synthesized CeO_2 with different morphologies and application in solvent-free benzyl alcohol oxidation. *Appl. Surf. Sci.* **2020**, *505*, 144473. [CrossRef]
40. Wang, D.; Zhu, Y.; Tian, C.; Wang, L.; Zhou, W.; Dong, Y.; Han, Q.; Liu, Y.; Yuan, F.; Fu, H. Synergistic effect of Mo_2N and Pt for promoted selective hydrogenation of cinnamaldehyde over Pt–Mo2N/SBA-15. *Catal. Sci. Technol.* **2016**, *6*, 2403–2412. [CrossRef]
41. Chen, C.; Wang, X.; Zhang, J.; Pan, S.; Bian, C.; Wang, L.; Chen, F.; Meng, X.; Zheng, X.; Gao, X.; et al. Superior Performance in Catalytic Combustion of Toluene over KZSM-5 Zeolite Supported Platinum Catalyst. *Catal. Lett.* **2014**, *144*, 1851–1859. [CrossRef]
42. Xiao, Z.; Xia, F.; Xu, L.; Wang, X.; Meng, J.; Wang, H.; Zhang, X.; Geng, L.; Wu, J.; Mai, L. Suppressing the Jahn–Teller Effect in Mn-Based Layered Oxide Cathode toward Long-Life Potassium-Ion Batteries. *Adv. Funct. Mater.* **2021**, *32*, 2108244. [CrossRef]
43. Zhang, C.; He, H.; Tanaka, K.-i. Catalytic performance and mechanism of a Pt/TiO_2 catalyst for the oxidation of formaldehyde at room temperature. *Appl. Catal. B: Environ.* **2006**, *65*, 37–43. [CrossRef]
44. Sun, B.; Xu, D.; Wang, Z.; Zhan, Y.; Zhang, K. Interfacial structure design for triboelectric nanogenerators. *Battery Energy* **2022**, *1*, 20220001. [CrossRef]
45. Wei, S.; Fu, X.P.; Wang, W.W.; Jin, Z.; Song, Q.S.; Jia, C.J. Au/TiO_2 Catalysts for CO Oxidation: Effect of Gold State to Reactivity. *J. Phys. Chem. C* **2018**, *122*, 4928–4936. [CrossRef]
46. Panagiotopoulou, P.; Christodoulakis, A.; Kondarides, D.I.; Boghosian, S. Particle size effects on the reducibility of titanium dioxide and its relation to the water–gas shift activity of Pt/TiO_2 catalysts. *J. Catal.* **2006**, *240*, 114–125. [CrossRef]
47. Wang, Y.; Pei, C.; Zhao, Z.J.; Gong, J. Kinetically rate-determining step modulation by metal—Support interactions for CO oxidation on Pt/CeO_2. *Sci. China Chem.* **2022**, *65*, 2038–2044. [CrossRef]
48. Zong, C.; Wang, C.; Hu, L.; Zhang, R.; Jiang, P.; Chen, J.; Wei, L.; Chen, Q. The Enhancement of the Catalytic Oxidation of CO on Ir/CeO(2) Nanojunctions. *Inorg. Chem.* **2019**, *58*, 14238–14243. [CrossRef]
49. Yao, Q.; Wang, C.; Wang, H.; Yan, H.; Lu, J. Revisiting the Au Particle Size Effect on TiO_2-Coated Au/TiO_2 Catalysts in CO Oxidation Reaction. *J. Phys. Chem. C* **2016**, *120*, 9174–9183. [CrossRef]
50. Zhen, J.; Wang, X.; Liu, D.; Wang, Z.; Li, J.; Wang, F.; Wang, Y.; Zhang, H. Mass production of Co_3O_4@CeO_2 core@shell nanowires for catalytic CO oxidation. *Nano Res.* **2015**, *8*, 1944–1955. [CrossRef]